Hierarchical and Multifunctional Three-dimensional Network of Carbon Nanotubes for Supercapacitor and Strain Sensor Applications

Haiwon Lee
HANYANG UNIVERSITY SEOUL CAMPUS

05/19/2016
Final Report

REPORT DOCUMENTATION PAGE

1. REPORT DATE *(DD-MM-YYYY)*	2. REPORT TYPE	3. DATES COVERED *(From - To)*
19-05-2016	Final	13-Jun-2012 to 12-Jun-2015

4. TITLE AND SUBTITLE	5a. CONTRACT NUMBER
Hierarchical and Multifunctional Three-dimensional Network of Carbon Nanotubes for Supercapacitor and Strain Sensor Applications	FA23861214044

5b. GRANT NUMBER

5c. PROGRAM ELEMENT NUMBER

6. AUTHOR(S)	5d. PROJECT NUMBER
Prof. Haiwon Lee	

5e. TASK NUMBER

5f. WORK UNIT NUMBER

7. PERFORMING ORGANIZATION NAME(S) AND ADDRESS(ES)	8. PERFORMING ORGANIZATION REPORT NUMBER
Hanyang University Haengdang-dong, Seongdong-gu Seoul 133-791 Korea (South)	N/A

9. SPONSORING/MONITORING AGENCY NAME(S) AND ADDRESS(ES)	10. SPONSOR/MONITOR'S ACRONYM(S)
AOARD UNIT 45002 APO AP 96338-5002	AOARD
	11. SPONSOR/MONITOR'S REPORT NUMBER(S)
	AOARD-124044

12. DISTRIBUTION/AVAILABILITY STATEMENT

Approved for public release.

13. SUPPLEMENTARY NOTES

14. ABSTRACT

A coaxial carbon nanotube/manganese oxide material (3DNC/MnO2) was fabricated by coating manganese oxide on silicon pillar array assisted three-dimensional network of carbon nanotubes (3DNC), which could be used as an electrode for supercapacitors. The 3DNC provides not only a conductive framework for deposition of MnO2, but also sufficient voids for ionic diffusion, which are benefit for the electrochemical performance. Compared with the CNTs/MnO2 on bared silicon substrates (2DNC/MnO2), the 3DNC/MnO2 showed better specific capacitance and cycling stability. When the loading time of MnO2 was 3 min, the specific capacitance of 3DNC/MnO2 at the scan rate of 10 mV/s could be 294 F/g. The charge–discharge cycle stability was shown with 96% specific capacitance retention even after 2000 charge–discharge cycles at 100 mV/s scan rate.

15. SUBJECT TERMS

Carbon nano tubes, Nanotechnology, supercapacitor

16. SECURITY CLASSIFICATION OF:			17. LIMITATION OF ABSTRACT	18. NUMBER OF PAGES	19a. NAME OF RESPONSIBLE PERSON
a. REPORT	b. ABSTRACT	c. THIS PAGE			Kenneth Caster, Ph.D.
U	U	U	UU	41	**19b. TELEPHONE NUMBER** *(Include area code)* +81-42-511-2000

Hierarchical and Multifunctional Three-dimensional Network of Carbon Nanotubes for Supercapacitor and Strain Sensor Applications

Name of Principal Investigator: Haiwon Lee

- e-mail address : haiwon@hanyang.ac.kr

- Institution: Hanyang University

- Mailing address: Department of Chemistry, Hanyang University, 17 Haengdang-dong, Seongdong-gu, Seoul 133-791, Korea

- Phone: +82-2-2220-0945

- Fax: +82-2-2296-0287

Period of Performance: 06/13/2012 – 06/12/2015

1. Hierarchical and Multifunctional Three-dimensional Network of Carbon Nanotubes for Supercapacitor Applications

1.1. Three-dimensional network of coaxial carbon nanotube/manganese dioxide electrode for supercapacitors

Abstract

A coaxial carbon nanotube/manganese oxide material (3DNC/MnO$_2$) was fabricated by coating manganese oxide on silicon pillar array assisted three-dimensional network of carbon nanotubes (3DNC), which could be used as an electrode for supercapacitors. The 3DNC provides not only a conductive framework for deposition of MnO$_2$, but also sufficient voids for ionic diffusion, which are benefit for the electrochemical performance. Compared with the CNTs/MnO$_2$ on bared silicon substrates (2DNC/MnO$_2$), the 3DNC/MnO$_2$ showed better specific capacitance and cycling stability. When the loading time of MnO$_2$ was 3 min, the specific capacitance of 3DNC/MnO$_2$ at the scan rate of 10 mV/s could be 294 F/g. The charge–discharge cycle stability was shown with 96% specific capacitance retention even after 2000 charge–discharge cycles at 100 mV/s scan rate.

Introduction

As one of the most promising electrochemical energy storage materials, manganese oxide-based materials, which are environmental friendly, low cost and widely available while with a high theoretical capacity of 1370 F/g, have attracted numerous research works during recent decades. 0D, 1D, 2D and 3D nanostructured MnO$_2$ with different morphologies have been developed as electrode materials and shown their advantages in charge storage capability. However, limited by the intrinsic poor electronic conductivity of MnO$_2$, their high rate charge-discharge performances were hard to sustain. To overcome this disadvantage, there are commonly preferred strategies: incorporating MnO$_2$ with other metal elements (Ni, Ru, Al, Sn and Pb etc.) or porous, high surface area and conductive nanoarchitectures such as carbonaceous sphere, carbon nanotubes, graphene and conductive polymers and etc. Among those strategies for advanced metal oxide-based hybrid

nanostructure design, both coaxial thin layer structure and ordered nanostructure arrays attracted most attention. As known from previous research works, only a very thin layer of metal oxide material (several tens of nanometers from the surface) participated in the redox reaction. Hence, coaxial thin layer structure could let cations intercalate into entire active materials and shorten electron transport distance. Ordered nanostructure arrays is also an excellent candidate not only providing a conductive path way for electron transport but also for resolving the ionic diffusion and transport issues of supercapacitor electrodes by shorter diffusion length in void volume. Consequently, longer life cycle and stronger volume retention during the charge and discharge process was obtained. Thus, it can be seen that a coaxial thin layer MnO_2 hybrid nanostructure array is necessary for high performance MnO_2 supercapacitors.

In our previous research works, a pillar structure assisted three-dimensional network of carbon nanotubes (3DNC) was developed. As demonstrated, 3DNC has a hierarchically arrayed structure with interconnected CNTs between ordered arrays of Si pillars. Because of its unique structural properties, 3DNC had been applied to many applications, such as catalysis, gas sensor, microfluidic platform, surface-enhanced Raman scattering etc. The CNTs suspended between ordered Si pillars are stable during electrochemical reactions and the 3DNC structure provides hierarchically controlled voids for ionic diffusion onto the surface of active materials. It would be meaningful to study the capacitance performance if such a 3D hierarchical structure incorporated with MnO_2 is used.

In this work, 3DNC coaxially coated with MnO_2 is used as an electrode for supercapacitor application. The 3DNC structure is not only served as a stable and conductive framework for controlled electrochemical deposition (ECD) of MnO_2 and a current collector for charge/discharge, but also provides sufficient voids for fast ionic transport between CNTs and ionic diffusion onto the surface of active materials. At the same time, the coated thin layer MnO_2 reduces the distance of ion diffusion and electron transport, enabling fast and reversible faradic reactions.

Experiment

Preparing of 3DNC/MnO₂ composites: Detailed preparing procedure has been explained in our previous works, and bared Si wafer (without etching process) was used for comparison.

Materials characterization and electrochemical evaluation: Sample morphologies were characterized by field-emission scanning electron microscope (FE-SEM, S-4800, Hitachi), transmission spectroscope (TEM, JEOL-2100F, JEOL), and X-ray photoelectron spectroscopy (Al Kα excitation laser, ESCA 2000). The electrochemical properties of samples were determined by cyclic voltammetry (CV). CV was carried out in the potential range of 0 to 0.8V at a scan rate of 10, 20, 50 and 100 mV/s. For the three-electrode configuration, standard calomel electrode (BASi, USA) was used as reference electrode, and Pt wire (>99%, Aldrich, USA) was used as counter electrode in 1M Na_2SO_4 aqueous solution (>99.9%, Aldrich). Life cycle tests were characterized by CV curves at a rate of 100 mV/s for 2000 cycles. The ohmic cell information was characterized by electrochemical impedance spectroscopy (AUT 302N, Autolab). The electrolyte and electrodes were the same as with the CV curve test. Solution resistance and charge transfer resistance were characterized over a frequency range from 100 kHz to 10 Hz at sinusoidal voltage amplitude of 5mV and room temperature.
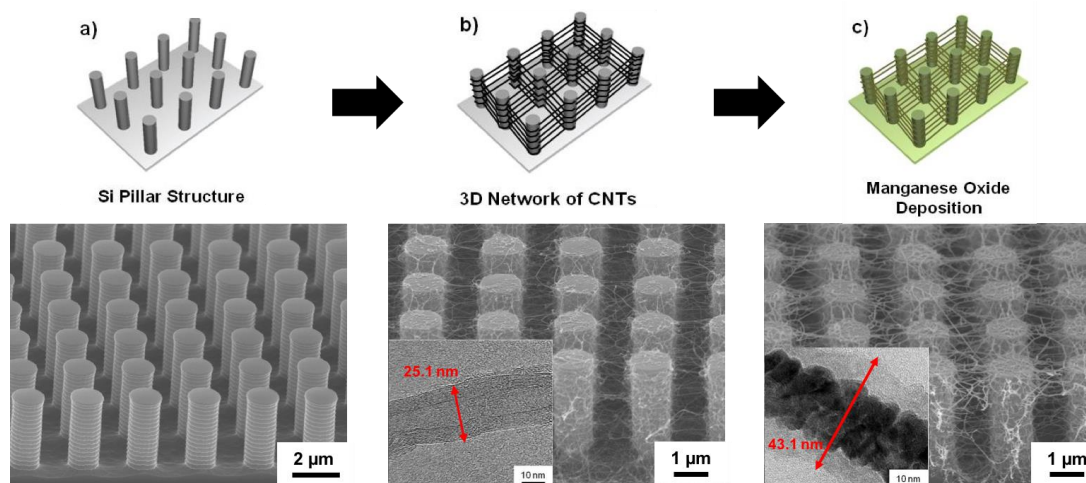

Figure 1-1. Schematic illustration of 3DNC/MnO₂ fabrication process and SEM images of (a) pristine Si pillar substrate; (b) as synthesized 3D network of CNTs (c) MnO₂ coated on 3D network of CNTs.

Results and Discussion

The synthesis process of 3DNC/MnO₂ is schematically illustrated and the corresponded scanning electron microscope (SEM) images are presented in Figure 1-1. The CNTs synthesized on bared wafer (2DNC) is processed in same condition for comparison. Figure 1-2 shows the 2DNC and 2DNC/MnO₂. Figure 1-1a shows a SEM image of Si pillar substrate. The diameter and

height of Si pillars were about 1.0 and 3.0μm, respectively. After synthesizing CNTs, most CNTs were tangled on both the sides and tops of pillars, and some CNTs were suspended between pillars as shown in figure 1-1b. The insert in figure 1-1b shows the TEM of synthesized multiwall CNTs. The average diameter is around 25.1nm. Figure 1-1c shows the SEM image of MnO_2 coated 3DNC. The original 3D network morphology is retained after MnO_2 deposition and the diameter of CNTs are increased obviously. The insert TEM image clearly presents Pt coated CNT backbone and a thin layer (thickness is around 5~10nm) of as coated amorphous MnO_2. The average diameter is around 43.1nm. The Pt played an important role in combining CNTs and target MnO_2. As demonstrated in previous work, Pt coating is an essential step to improve the mechanical strength and maintaining the morphology of the 3DNC structures as well as enhancing electron transportation and adhesion between 3DNC and MnO_2.
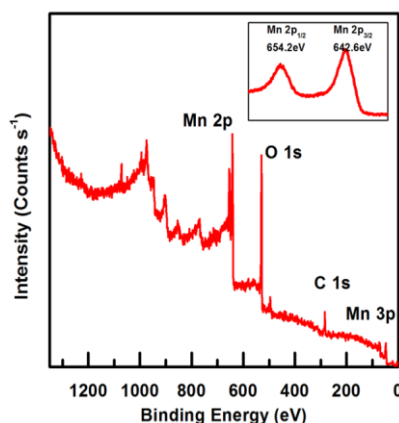

Figure 1-2. XPS spectrum of 3DNC/MnO_2.

3DNC/MnO_2 was characterized by X-ray photoelectron spectroscopy (XPS) for a better understanding of the chemical composition and oxidation state of Mn. Figure 1-2 shows the XPS spectrum of 3DNC/MnO_2, and peaks of Mn 2p, O 1s, and C 1s are observed. The insert shows two peaks located at 654.2eV and 642.6eV, which are attributed to Mn $2p_{1/2}$ and Mn $2p_{3/2}$, respectively. Those results are in agreement with previously reported data and indicating an oxidation state of Mn^{4+}.
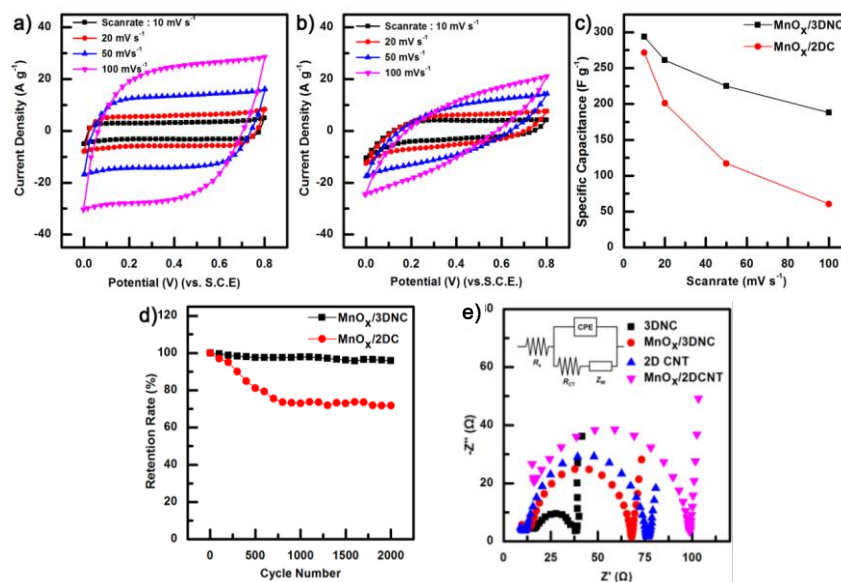
Figure 1-3. CV curves of 3DNC/MnO₂ (a) and 2DNC/MnO₂ (b) at scan rate of 10, 20, 50 and 100 mV/s in 1M Na₂SO₄ solution. (c) Specific capacitance of 3DNC/MnO₂ and 2DNC/MnO₂. (d) Retention graph during 2000 cycles at scan rate of 100 mV/s. (e) Nyquist plots of 3DNC, 3DNC/MnO₂, 2DNC, and 2DNC/MnO₂.

CV measurement of 3DNC/MnO₂ and 2DNC/MnO₂ at scan rates of 10, 20, 50 and 100 mV/s were investigated. The CV curves of 3DNC/MnO₂ (Figure 1-3a) are closer to a rectangular shape and a mirror image at each scan rate than those of 2DNC/MnO₂ (Figure 1-3b). The shape of 3DNC/MnO₂ CV curves did not change significantly while scan rate increasing, so 3DNC/MnO₂ provided better capacitive behavior.

Figure 1-3c shows specific capacitance (C_{sp}) retention at different scan rates. The calculated C_{sp} values of 3DNC/MnO₂ are 294, 261, 225 and 188 F/g at scan rates of 10, 20, 50 and 100 mV/s respectively, whereas the calculated C_{sp} values of 2DNC/MnO₂ are 271, 201, 117 and 60 F/g. The C_{sp} value difference of both structures is not so much at a low scan rate, like 10 mV/s. However, when scan rate increases, the C_{sp} value of 2DNC/MnO₂ decreased more dramatically than 3DNC/MnO₂. By comparing the SEM images of 3DNC/MnO₂ (Figure 1-1c) and 2DNC/MnO₂ (Figure 1-4b), the CNTs on 2DNC/MnO₂ are tightly connected or touched with adjacent ones compared with the CNTs on 3DNC/MnO₂. That means the voids in 3DNC/MnO₂ are larger than that in 2DNC/MnO₂. Consequently, larger voids promoted the ion diffusion and transfer between electrolyte and electrode and improved the capacitive performance.

The cyclability was confirmed by 2000 cycles at scan rate of 100 mV/s. Figure 1-3d shows the life cycle test of 3DNC/MnO₂ and 2DNC/MnO₂. The C_{sp} of 3DNC/MnO₂ retains about 96%

DISTRIBUTION A: Approved for public release: distribution unlimited.

capacitance even after 2000 cycles while 2DNC/MnO$_2$ retains only 72%. 3DNC/MnO$_2$ shows better stability and reversible capacitive behavior even at high charging/discharging rates.

Table 1. Fitting values of the equivalent circuit elements of Faradic charge transfer resistance (R_{ct}) and Warburg resistance (Z_w).

Parameters	Electrode material			
	3DNC	3DNC/MnO$_2$	2DNC	3DNC/MnO$_2$
R_{CT}	23.6	54.9	65.5	82.8
Z_W	11.7	11.9	15.3	20.3

In addition, electrochemical impedance spectroscopy (EIS) was also carried out to understand the electrode resistance and ion-transfer behavior of the electrode materials (Figure 1-3f). The proposed equivalent circuit for the measured impedance data is shown in the inset of Figure 1-3e, where R_s is the internal resistance, R_{ct} is Faradic charge transfer resistance, *CPE* is the double-layer capacitance, Z_w is the Warburg resistance. Typically, the semi-circle in medium frequency regions reflects the R_{ct}. Before coating MnO$_2$, the R_{ct} value of 3DNC (23.6Ω) was much smaller than that of the 2DNC electrode (65.5Ω). It should be attributed to the 3D network of 3DNC, which benefits the charge transfer between the electrode surface and the electrolyte. After coating MnO$_2$, the R_{ct} of 3DNC/MnO$_2$ and 2DNC/MnO$_2$ increased to 54.9Ω and 82.8Ω due to the poor conductivity of MnO$_2$. However, the R_{ct} value of 3DNC/MnO$_2$ was also much smaller than that of the 2DNC/MnO$_2$ electrode.

In the low frequency region, the slope of the curve represents the Z_w, which is related to electrolyte diffusion in the porous electrode and proton diffusion in the active materials. [24] The Z_w value of 3DNC (11.7Ω) and 3DNC/MnO$_2$ (11.9Ω) were smaller than those of the 2DNC (15.3Ω) and 2DNC/MnO$_2$ (20.3Ω) electrode. The results were due to the unique structure based on Si pillar wafer, which provided better electrolyte ion diffusion during fast charge and discharge processes.
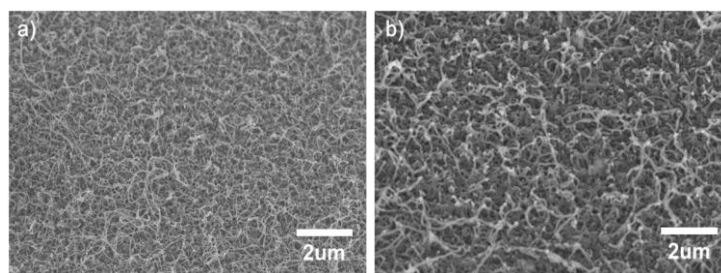
Figure 1-4. SEM images of (a) CNTs grown on flat Si template, (b) manganese oxide deposited CNTs on Si.

1.2.   Polyaniline/3DNC for supercapacitor application

Abstract

Polyaniline (PANI) was successfully combined with 3DNC as supercapacitor electrodes by two commonly used method: chemical polymerization (CP) and electrochemical deposition (ECD). The combination of PANI and the 3DNC led to a fascinating result, showing high specific capacitance of 615 F/g (CP) and 1120 F/g (ECD) at the current density of 10 A/g. Both electrodes showed stable electrochemical performances at different CV scanning rate and charging-discharging current. CP synthesized 3DNC/PANI electrode showed long cycle ability of 20.73% loss of specific capacitance after 3000 cycles.

Introduction

Conducting polymers have been regarded as other promising pseudo-capacitive materials. The use of conducting polymer materials for redox supercapacitors has several advantages over other systems. The materials have good intrinsic auto-conductivity and are relatively cheap, so the preparation and fabrication costs would be competitive. In addition, good specific capacitance can be obtained and existing battery-type technology for fabrication procedures may be used. Among them, polyaniline has attracted much attention because of higher environmental stability, controllable electrical conductivity, and easy processability. It would be meaningful to study the capacitance performance if our 3D hierarchical structure incorporated with PANI.

In this work, 3DNC coated with PANI is used as an electrode for supercapacitor application. Chemical polymerization (CP) and electrochemical deposition (ECD) of PANI on 3DNC was investigated. The 3DNC structure is not only served as a stable and conductive framework for controlled deposition of PANI and a current collector for charge/discharge, but also provides sufficient voids for fast ionic transport between CNTs and ionic diffusion onto the surface of active materials. Not only for these advantages, PANI has been adopted to 3D network of CNTs substrate due to its synergistic effect derived from specific interaction between PANI and CNT composite in terms of enhanced life cycle with mechanical support of CNTs and high surface-area morphology for efficient utilization of electrode materials. In addition, coating PANI on suspended CNT network overcome the limitation of previously reported method, irregular alignment and dispersion of CNTs dissolved in solution based chemical reaction fabrication process which lead to low scalability and efficiency due to lots of boundaries and poor ion diffusivity.

Experiment

Preparation of 3D network of CNTs on Si substrate: Pillars arrayed Si substrate was fabricated on Si (100) wafers (N-doped, 0.01-0.02 Ω). CNT was directly synthesized on the substrate using thermal chemical vapor deposition method.

PANI coating on 3DNC: (1) PANI was coated by dipping method in solution. Firstly, the 3DNC was dipped in aniline solution made of 0.025 ml aniline monomer and 12 ml 1M H2SO4. After 20 minutes, 0.018 g of ammonium persulfate (APS) was dissolved as an initiator of polymerization. The solution was kept in ice bath at 3 ℃. After 75 minutes since APS is added, the template was taken out from the solution and rinsed with tetra hydrofuran (THF) solution for several seconds. (1) PANI was coated by ECD method. The substrate was carefully immersed into aqueous solution containing 0.1 mol/L aniline and 1 mol/L H_2SO_4 under pulse static potential. A core-shell structure of CNT/PANI was well synthesized by controlling the polymerization parameters , such as anodic pulse duration (t_a), cathodic pulse duration (t_c), lower limit potential (E_c) and upper limit potential (E_a).

Under the following conditions of $t_a = 1$ s, $t_c = 4$ s, $E_c = -0.2$ V and $E_a = 0.82$ V, the high quality of 3DNC/PANI sample was obtained.

Characterization of 3DNC/PANI bundle: The morphologies of samples were characterized by field-emission scanning electron microscope (SEM, S-4800, Hitachi). The chemical composition of the sample was investigated with RAMAN spectroscopy (LabRam Aramis, 514 nm laser excitation waverlength, Jobin Yvon). The electrochemical properties of the samples were determined by cyclic voltammetry (CV) and galvano-static charge/discharge using a potentiostat/galvanostat in a three-electrode system (WPG100, WonAtech). Platinum wire and S.C.E. were used as counter electrode and reference electrode. 1 M H2SO4 solution was used as an electrolyte. The voltage ranges for CV and CD were -0.2-0.6 V and 0-0.6 V, respectively.

Results and discussion

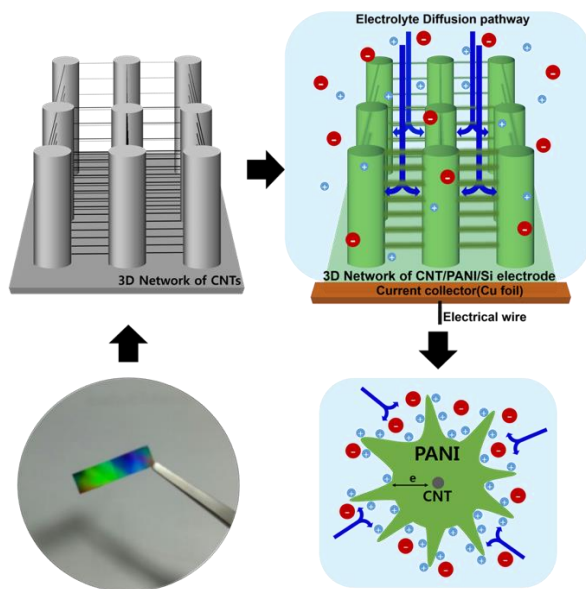### 1.2.1. **PANI coating on 3DNC by chemical polymerization method**

Figure 1-5. **Schematic illustration of a fabrication process for 3DNC/PANI and charging/discharging mechanism of the electrode with electrolyte ions.**

Figure 1-5 shows the experimental procedure of fabrication of 3DNC/PANI Si supercapacitor electrode. The fabrication process of 3D network of CNTs on Si substrate was described in

previous report in detail. In this study, CNTs are synthesized on Si substrate which is having height, diameter, and interval of each pillar was 5um, 1um, and 1um. As patterned pillar diameter, height, and gap are controllable, further study could be conducted systematically investigating how these factors influence on ion-diffusion and charging-discharging mechanism of well-ordered 3D architecture electrode system. The as-grown 3DNC has suspended CNTs mainly between adjacent pillars.
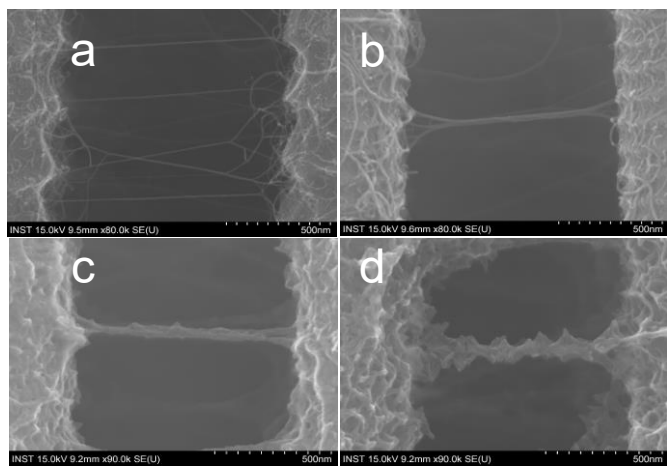

Figure 1-6. SEM images of 3DNC coated with PANI in different polymerization time. (a) Before dipping, (b) 1 minute after dipping, (c) 40 minutes after dipping and (d) 75 minutes after dipping.

The overall CNT networks were interconnected and could working as a conducting path, which reduce the resistance of Si based electrode. Additionally, this 3D network work as bridging skeleton structure between Si pillars, enlarging surface area in a scalable way. After the successful fabrication of 3D network of CNTs on Si substrate, the substrate was carefully merged into aniline monomer dissolving solution for coating PANI on 3D network of CNTs substrate. To investigate the overall growth mechanism of PANI on 3D network of CNTs, total 4 SEM images in different dipping time were taken (Figure 1-6). Right after the substrate was dipped in the solution, each suspended CNTs nearby the region of pillar sidewall were agglomerated and formed a bundle of CNTs due to hydrophobicity and pi-pi interaction between adjacent CNT's graphitic sidewall, accelerated by fluctuation of solution fluid. After APS treatment, PANI was grown on CNTs showing protuberances on the bundle. This protuberance induced the further growth of PANI on each sites, and finally nanorod-like PANI structure was formed on each CNT bundle. This 3D network of CNTs coated with nanorod-like PANI dramatically increased the surface area. SEM images of 3D network of CNT/PANI on Si substrate were shown in Figure 1-7.

To investigate and compare the advantages of 3D network structure, 2D CNT/PANI Si electrode was fabricated on a flat Si substrate via the same procedure with that mentioned above. The chemical composition analysis of 3DNC/PANI Si substrate was conducted by Raman spectroscopy as shown in Figure 1-8. Each peak of the spectrum clearly shows that PANI is covering CNT bundles by showing the representative peaks of both CNT and PANI in the same spectrum. Cyclclic voltametry (CV) test was conducted to figure out the electrochemical performance of the electrode material. Figure 1-12 shows the CV curves of 2D and 3D CNT/PANI Si electrodes in 1M H_2SO_4 solution at different scan rates. To avoid the dissolution of PANI in
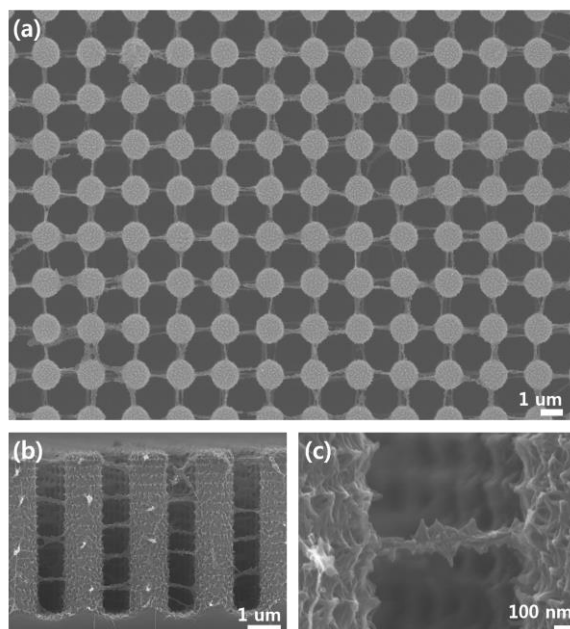

Figure 1-7. SEM images of 3DNC coated with PANI. (a) Top view (b) Cross section view and (c) Close view of PANI/CNT bundle suspended between two pillars.

H_2SO_4 electrolyte induced by the oxidation of emeraldine to pernigraniline at near 0.7V, potential range was set within -0.2 to 0.6V. To investigate the effect of scan rate on CV response of the 2D and 3D CNT/PANI Si electrode, several scan rate was choosed. Figure 1-9 reveals that both 2D and 3D CNT/PANI electrodes showed typical characteristics of PANI. Both CV curves showed a redox peaks (C1/A1) of transition from leucoemeraldine to the polaronic emeraldine. As the scan rate increased, the cathodic and anodic peaks of both 2D and 3D CV curves shifted positive and negative shift respectively, with increasing current intensity. However, 3D showed greater rate capability and reversibility, as CV curve maintained its mirror-image shape regarding the zero current even in higher range of scan rate (10 mVs^{-1} - 300 mVs^{-1}) while the shape of CV curves of

2D structure changed significantly in lower range of scan rate (5 mVs^{-1} - 50mVs^{-1}). This outstanding response capability to fast voltage scan is probably caused by the fast ion-diffusion process facilitated by regularly ordered 3D structure, while the rate of diffusion of ion cannot follow up the rate of charge transportation in 2D structure. Figure 1-9(C) shows the CV curves of 2D and 3D structure at the scan rate of 5 mVs^{-1}. The total current density of 3D structure larger than 2D structure. This could be explained by the enlarged electrode/electrolyte contact area of same amount of PANI in 3D network structure in the space, enables a large amount of redox reaction within the limited time. In order to study a possible application as supercapacitor electrode, gavalnostatic charging and discharging of the 3DSi/NT/PANi at different current densities were examined. The Figure 1-9(b) shows nearly a symmetrical shape of charge and corresponding discharge curve, which indicates that the charge and discharge process of the electrode is highly reversible. However, a large amount of voltage drop at the beginning of discharging curve was observed in 2DNC/PANI electrode (Figure 1-9(a)). In addition, the range of current that electrodes could be exposed for charging cycle for 3DNC/PANI and 2DNC/PANI were 3-10 A/g and 10-200 A/g each, indicating that the 3DNC/PANI can experience much wider range of current. This results could be explained by the hierarchical 3D structure of electrode, which enables fast ion-diffusion and large contact area between electrode and electrolyte. The discharging time is shorter than the charging time, indicating a loss of capacity duing the redox reaction. The specific capacitance based on the mass of electroactive material was calculated from the galvanostatic discharge curve with following equation Cs = IΔt/mΔV, where I is the charge-discharge current, Δt is the discharge time, ΔV is the voltage drop during discharge process, and m is the mass of electroactive materials. The specific capacitance of 3DNC/PANI were 615, 576.7, 520.8, 466.7, 366.7 at the current density of 10, 20, 50, 100, 200 A/g. The specific capacitance of 2DNC/PANI was 380, 288.3, 198.3, 116.7 at the current density of 3, 5, 7, 10 A/g each. The charge-discharge curve of 3DNC/PANI and 2DNC/PANI at same current density was investigated at Figure 1-9(c). The results clearly shows that 3DNC/PANI has lower internal resistant value (R). Also, the specific capacitance value of 3DNC/PANI was 2.04 times higher than that of 2DNC/PANI. Figure 1-10 shows the retention ratio of specific capacitance and coulomb efficiency of 3DNC/PANI with increasing number of cycles. Consecutive charge-discharge cycles are repeated at a current density of 10Ag^{-1} for 3000 times. The electrochemical redox mechanism is mainly caused by faradaic reaction of PANI and electrolyte ions. The gradual decrease of specific

capacitance of the electrode could be explained by continuous loss of electrical contact between CNT and PANI, as disintegration of electrode is known to occur with swelling and shrinking in each doping/dedoping process cycle. After 3000 consecutive cycles, specific capacitance value was retained of 79.26%. Figure 1-10 also shows retention of the Coulomb efficiency (n) calculated by following equation: n (%) = $(t_d/t_c) * 100$ where t_d and t_c are discharge and charge times. As PANI/CNT supercapacitor electrode was reported for having high and stable Coulomb efficiency, the result revealed that 3D CNT/PANI electrode maintained about 100% over 3000 cycles.

Figure 1-8. Raman spectra of (from the lowest) bare Si wafer, CNT grown Si wafer, pristine PANI powder, and PANI coated CNT Si wafer.
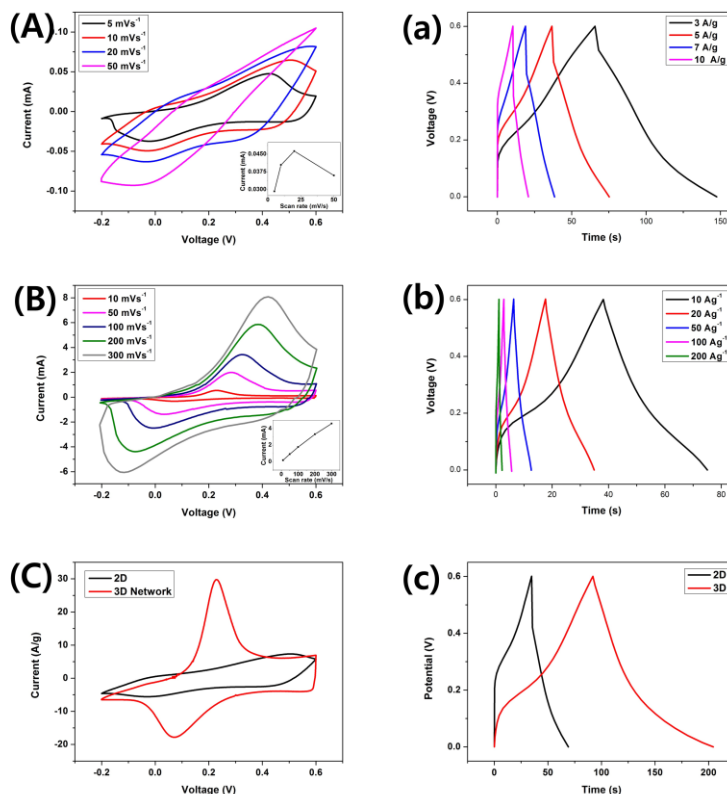
Figure 1-9. (Left row) CV curves of (A) 2DNC/PANI (B) 3DNC/PANI (C) 2DNC/PANI and 3DNC/PANI at the scan rate of 10 mV/s. (Right row) (a) Galvanostatic charge-discharge curve of (a) 2DNC/PANI (b) 3DNC/PANI (c) 2DNC/PANI and 3DNC/PANI at the current density of 5 A/g .
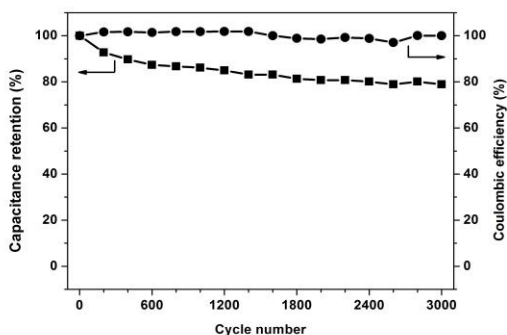

Figure 1-10. Retention ratio of specific capacitance and columbic efficiency over 3000 charge-discharge cycles.

However, the SEM of the samples after life-cycle tests indicated that the morphology of PANI became rather smooth as shown in Figure 1-11c and 11d Even the surface area after a life cycle test is rather smaller than the one before a life cycle test, depending on the capacitance retention

plot in Figure 1-11e, its specific capacitance is still very high. Although vertical PANI nano-rods (Figure 1-11a and 11b) greatly increase the specific surface area, they also enlarged the charge transport distance from PANI surface to inner CNT surface. After a life-cycle, the diameter of PANI/CNT was decreased, and it reduced the ionic diffusion resistance and the charge transfer resistance. Hence, the surface morphology of PANI nano-rods in 3DNC system is not critical for realizing the efficient utilization of the electrode materials.

Figure 1-11. SEM images of 3DNC/PANI before and after life-cycle tests. (a) and (b) are before a life-cycle test; (c) and (d) are after a life-cycle test.

1.2.2. PANI coating on 3DNC by ECD method

Here we report a new method of the preparation of 3DNC/PANI core-shell structure by using electrochemical synthesis for improving the specific capacitance performance as a supercapacitor electrode. And also the properties of samples prepared by both electrochemical method and chemical method were compared. The pulse method was used for the electrosynthesis of PANI film on 3DNC as illustrated in Figure 1-12. The periodic pulses with lower limit potential E_c and upper limit potential E_a, and cathodic pulse duration t_c and anodic pulse duration t_a were applied continuously at a given experimental time t_{exp}. The overall oxidation time t_{ox} can be calculated from the following equation:

$$t_{ox} = t_{exp} \frac{t_a}{t_a + t_c}$$

(1)

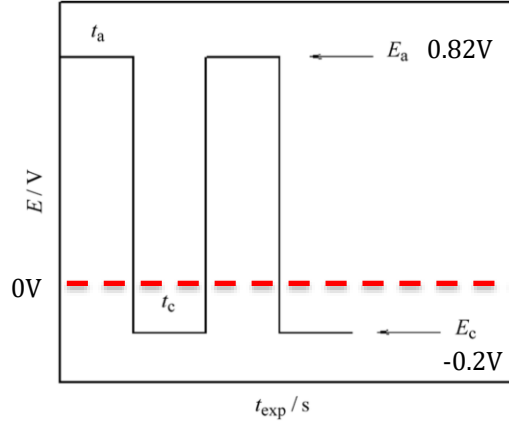**DISTRIBUTION A: Approved for public release: distribution unlimited.**

Figure 1-12. Schematic principle of pulse potentiostatic method.

To investigate the best electro-activity of 3DNC/PANI, different electropolymerization times were taken from 60s to 180s. By increasing the coating time, the mount of polymerized PANI increases linearly by a fitting equation:

$$T= -12.36 + 1.05*t_{ox} \qquad (2)$$

where T is the diameter of PANI/CNT, and t_{ox} is the overall oxidation time. When t_{ox} is 90s, PANI was uniformly well coated on the CNT surface with a diameter ~82 nm. With increasing the coating time, the mount of coated PANI increased significantly and it may be attributed from the enhanced conductivity caused by coated PANI.
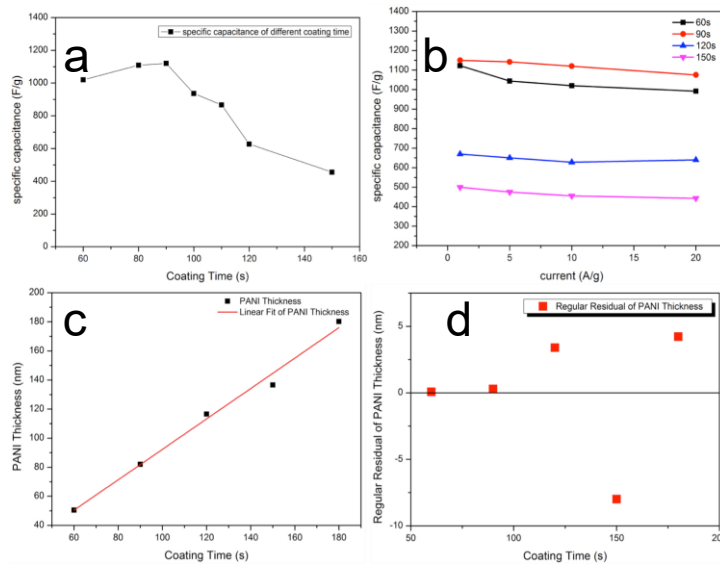
DISTRIBUTION A: Approved for public release: distribution unlimited.

Figure 1-13. (a) specific capacitance at 10A/g of 3DNC/PANI with different t_{ox}; (b) specific capacitance of different t_{ox} at 1, 5, 10, and 20 A/g; (c) linear fit of PANI/CNT and (d) regular residual of PANI/CNT.

CV and charge-discharge tests were conducted to figure out the electrochemical performance of the electrode materials. Figure 1-15A-15C show the CV curves of 3DNC/PANI electrodes in 1M H_2SO_4 solution at different scan rates. To avoide the dissolution of PANI in H_2SO_4 electrolyte enduced by the oxidation of emeraldine to pernigraniline at near 0.7V, the potential range was set within -0.2 to 0.6V. Both CV curves showed redox peaks of transition from leucoemeraldine (semiconducting state) to the polaronic emeraldine (conducting sate). As the scan rate increases, the cathodic and anodic peaks show positive and negative shifts with increasing current intensity, respectively. At $t_{ox=90s}$, the sample showed greater rate capability and reversibility, as the CV curve maintained its mirror-image shape regarding the zero current even in higher range of scan rate (10 mV/s ~ 500 mV/s). This outstanding response capability to the fast voltage scan is probably caused by the fast ion-diffusion process facilitated by regularly ordered 3D structure, while the rate of diffusion of ion cannot follow up the rate of charge transportation in t_{ox}=120s and t_{ox}=150s samples.
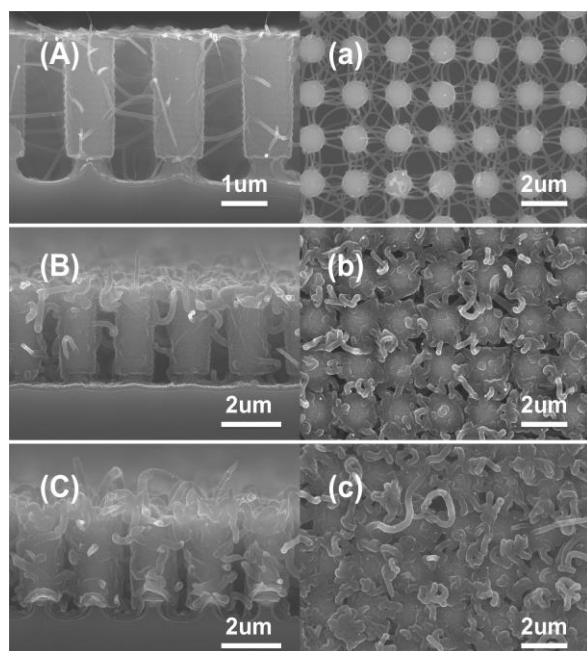

Figure 1-14. SEM images of 3DNC/PANI at different polymerization time. (A, a) t_{ox} = 90s; (B, b) t_{ox} = 120s; (C, c) t_{ox} = 150s.

In order to confirm a capability of possible application as supercapacitor electrode, gavalnostatic charging and discharging of the 3DNC/PANI at different current densities were examinedin Figure 1-15a-15c. Nearly symmetrical shape of charge and corresponding discharge curves was observed, which indicates that the charge and discharge processes are highly reversible. This excellent reversibility could be attributed by the hierarchical 3D structure of electrode because of fast ion diffusion/penetration and a large contact area between electrode and electrolyte. The discharging time is shorter than the charging time and it indicates a loss of capacity while the redox reaction.

The specific capacitance based on the mass of electroactive material was calculated from the galvanostatic discharge curve with following equation Cs = IΔt/mΔV, where I is the charge-discharge current, Δt is the discharge time, ΔV is the voltage drop during discharge process, and m is the mass of electroactive materials. The specific capacitances of 3DNC/PANI at t_{OX} = 90s were 1150, 1142, 1120, 1075 F/g at the current density of 1, 5, 10, 20 A/g, while the specific capacitances of 120s and 150s coated sample were only 670 and 500 F/g at the current density of 1 A/g in Figure 1-13b. The cycle-life characteristics of 3DNC/PANI is shown in Figure 1-16 .
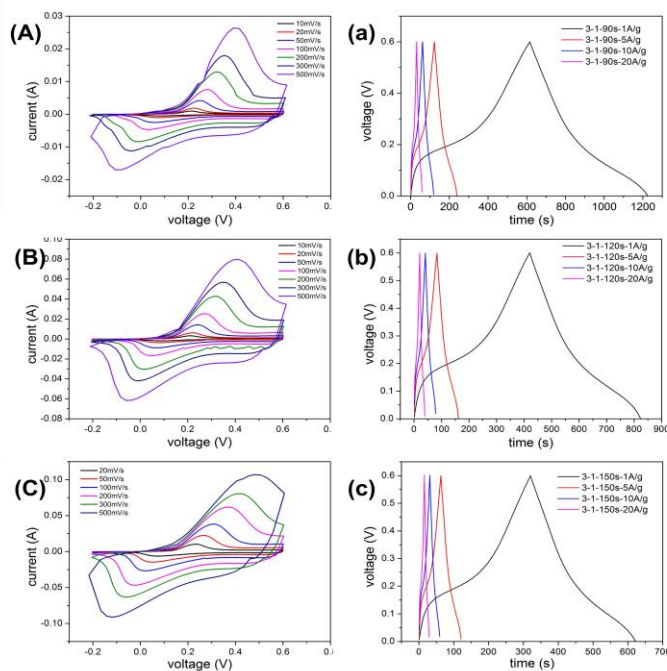

Figure 1-15. CV curves at the scanning rate from 10mV/s to 500mV/s of (A) t_{OX} = 90s, (B) t_{OX} = 120s and (C) t_{OX} = 150s 3DNC/PANI. Galvanostatic charge-discharge curve from 1A/g to 20A/g of (a) t_{OX} = 90s, (b) t_{OX} = 120s and (c) t_{OX} = 150s 3DNC/PANI.

In order to understand the electrochemical stability of the 3DNC/PANI electrode, consecutive charge–discharge cycles were measured with t_{ox} = 90s sample at a current density of 10 A/g (Figure 1-16b) and 100 A/g (Figure 1-16a). The 3DNC/PANI electrode was shown to keep only 68.78% of its initial capacitance after 3000 cycles at 100A/g. To compare with our previous data, all samples were tested at 10A/g. The retention was 85.47% after 400 cycles and went up gradually until 1292th cycles with a value of 829.47%, which means the performance of 3DNC/PANI had been abnormal. Figure 1-16c showed the 1291 cycle charge-discharge curve. Discharging time was much larger than charging time. SEM image shows the morphology of 3DNC/PANI after 1292cycles at 10A/g in Figure 1-16d. Numerous unknown particles were generated on the PANI/CNT surface. The reason for forming those particles is not confirmed yet, but by comparing with Figure 1-11c and 11d we can guess the reason of poor performance may come from those particles. By referring electrochemical test processes under N_2 atmosphere in reference, the formation of those particles may be attributed from the oxidation between PANI and O_2 dissolved in the electrolyte.

Hence further investigation of the identification of those particles and improvement of 3DNC/PANI stability will be carried out.
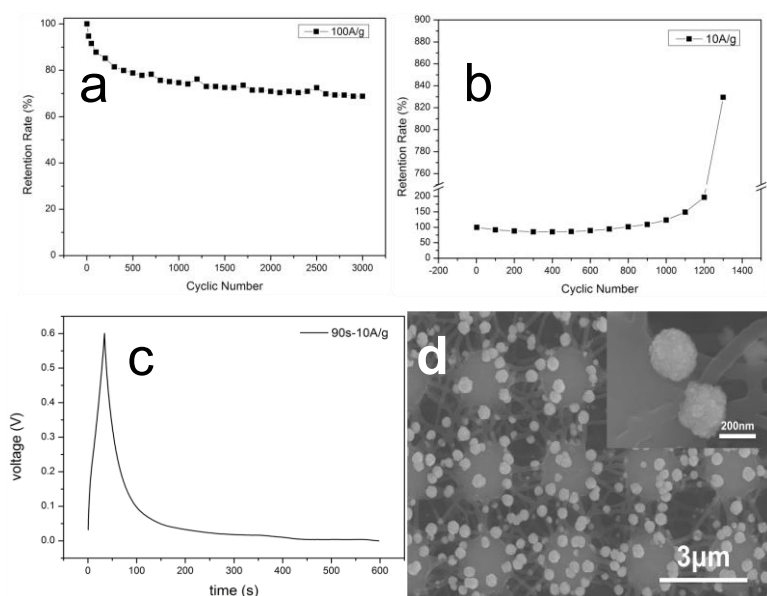

Figure 1-16. (a) retention ratio of specific capacitance over 3000 charge-discharge cycles at 100A/g; (b) retention ratio of specific capacitance at 10A/g; (c) galvanostatic charge-discharge curve of 1291th cycle at 10A/g; (d) SEM images of 3DNC/PANI after a life-cycle test.

2. Hierarchical and Multifunctional Three-dimensional Network of Carbon Nanotubes for Strain Sensor Application

Abstract

 w\e leveraged a 3D network of single-walled carbon nanotubes (SWNTs) embedded in poly(dimethylsiloxane) (PDMS) for use as a strain sensor using as-grown SWNTs on Si pillars. The Si pillars were introduced as a template for the fabrication of an ordered 3D network arrangement as well as supporting the electrical connection between embedded SWNTs. This is the new approach for the directional alignment of SWNTs in PDMS. In particular, the influence of various parameters on the piezoresistance change was examined through an analysis of the Raman shift and $\Delta R/R_0$ at various applied strains. This hierarchical 3D network of SWNTs embedded in a PDMS film can be used to reveal a wide range of sensitive applications needing precision as in wearable electronics, robotics and health care.

Introduction

Carbon nanotubes (CNTs) is an excellent candidate for flexible devices and sensors because of their high strength, flexibility, and stability. In functional composites, for example, it is possible to produce elastic conductive films by dispersing CNTs in elastomeric polymers or forming CNTs on elastomeric polymers. When CNTs are introduced into a polymer matrix to form electrical pathways, the resistance change in the composite itself can be monitored and thus, the strain under an applied load can be measured. These electrically conductive films can be employed to measure the strain dependent change in device performance and monitor motion. However, an embedded sensor has detrimental effects on the integrity of the structure and the implementation of complex equipment remains a technical challenge for field applications.

Since CNTs have a one-dimensional structure, their alignment is able to significantly affect the electrical and mechanical properties of the sensor. For example, sensor sensitivity is highly related to the electrical percolation phenomenon of CNTs. Percolation describes the long range connectivity of CNTs. The fabrication of low percolation threshold composites has been

investigated to increase sensitivity. To achieve a low percolation threshold, it is preferable that the CNTs in composites are arranged in a straight network and have a high aspect ratio (L/D) and low aggregation. Previous CNTs sensors were based on the random network of CNTs comprised of 2D CNT sheets or CNT/polymer composites. However, the strong van der Waals forces of CNTs lead to difficulties in producing a homogeneous network structure. The random network causes deterioration of the electrical conductivity and irrecoverable loss of junctions among CNTs when repetitive strain is applied to the film. Furthermore, various surfactants, mixing parameters, and CNT volume fractions have been considered to improve the CNT dispersion.

In this regard, Jung et al. reported a directional alignment of carbon nanotubes in polymer matrices by incorporating aligned and patterned CNTs into a soft poly(dimethylsiloxane) (PDMS) matrix. The as-grown CNT architecture on a substrate was transferred into the PDMS matrix without disturbing the CNT alignment. However, the composite film was more sensitive to compression strain than to tensile strain because the resistance change by strain was attributed to a change in the contact area between aligned CNTs.

In this work, we leveraged a film of three-dimensional (3D) network of SWNTs embedded in PDMS to develop a flexible strain sensor. This is the first demonstration of a three-dimensionally ordered SWNT network transferred to a flexible strain sensor.

Experiment

Preparation of Si pillar arrays: The Si pillar template was fabricated on a highly doped n-type Si (100) substrate using a photolithography technique which included a deep Si etching process (SLR-770-10R-B, Plasma Thermo Co.). The diameter and height of the as-prepared Si pillars were 1 and 3µm, respectively.

Formation of catalyst on template: A Fe-Mo catalyst solution was prepared by ultrasonication using $Fe(NO_3)_3 \cdot 9H_2O$ (Junsei) and Mo solution (ICP/DCP standard solution, Aldrich) in ethanol solvent. The molar ratio of Fe/Mo in the catalyst solution was 7/1. To form the Fe-Mo catalyst nanoparticles on the Si pillar template, the substrate was soaked in the Fe-Mo catalyst solution for 60 minutes followed by rinsing with ethanol. As a result, Fe-Mo catalyst nanoparticles were uniformly formed over the entire surface area of the Si pillar template.

Synthesis of 3D SWNTs network: 3D SWNT network was grown on Si pillars substrates using thermal chemical vapor deposition (CVD) of C_2H_2 at 800℃. PDMS pre-polymer solution, a viscous mixture of base/curing agent (weight ratio of 10:1), is poured over the SWNTs network structures on the substrate. Any excessive PDMS solution is removed carefully to obtain the optimum thickness for a SWNT/PDMS composite film. The PDMS is then thermally cured at 100 ℃ for 1 h and subsequently, networked SWNT/PDMS composite films are peeled off from the Si substrate carefully.

Fabrication of strain sensor: 3D network of SWNTs/PDMS composite film was cut into small rectangles. (2.0 x 1.0 cm^2). And then 20nm/80nm thickness Cr/Au metal electrodes are fabricated on the PDMS/SWNT composite film by depositing Cr and Au using thermal evaporation method, respectively. Electrical contacts were established by drying silver paste under aluminum sheet to form a two alligator probe measurement setup. For measuring electrical characteristics SWNT/PDMS composite film was loaded in a load frame. And then, load frame applied to slow tensile strain and released load patterns to the SWNT/PDMS composite film for 20 seconds. Resistance changed under applied cyclic loading was sampled at 1 voltage using a Keithley 2400 source meter supplying direct current.

Characterization: The morphologies of samples were characterized by field-emission scanning electron microscope (FE-SEM, Hitachi), transmission spectroscope (TEM, JEOL-2100F), and Raman spectroscopy (LabRam HR, 514 nm laser excitation wavelength, Jobin-Yvon).

Results and Discussion

A schematic illustration of the steps involved in the fabrication of a strain sensor based on an embedded 3D network of SWNTs in PDMS is shown in Figure 2-1. The fabrication of 3D networks of SWNTs was detailed in our previous report. Initially, a Si pillar template (height: 3 μm, diameter: 1 μm, gap: 1 μm) was fabricated on a Si substrate via photolithography. The PDMS was thermally cured and the embedded 3D network of SWNTs in the PDMS film was peeled off from the Si pillar substrate. To measure the resistance of the film with respect to the tensile strain, Au was thermally evaporated to form metal electrodes on the embedded 3D network of SWNTs in the PDMS film. As shown in Figure 2-1f, the fabricated strain sensor was flexible.
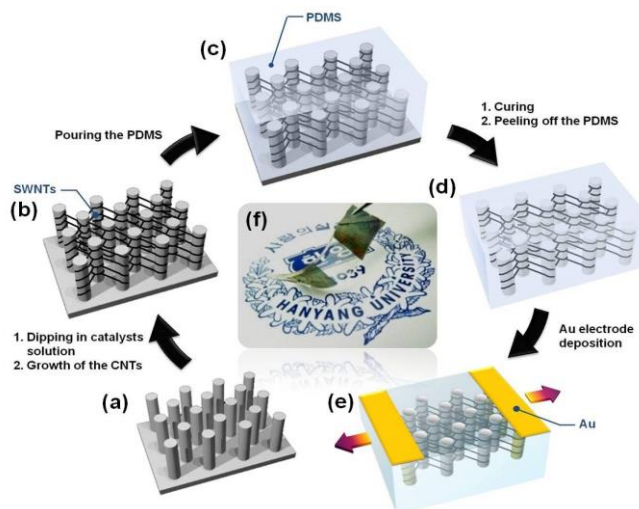
Figure 2-1. Schematics illustrating the strain sensor fabrication process from a 3D network of SWNTs (3DNS). (a) Si pillar substrate; (b) growing a 3DNS on the pillar structure; (c) pouring molten PDMS onto the 3DNS; and (d) peeling of the 3DNS in PDMS from the pillar template. (e) Formation of metal electrodes and resistance measurement of the film with respect to the tensile strain. (f) Image of the transparent, stretchable 3DNS in PDMS.
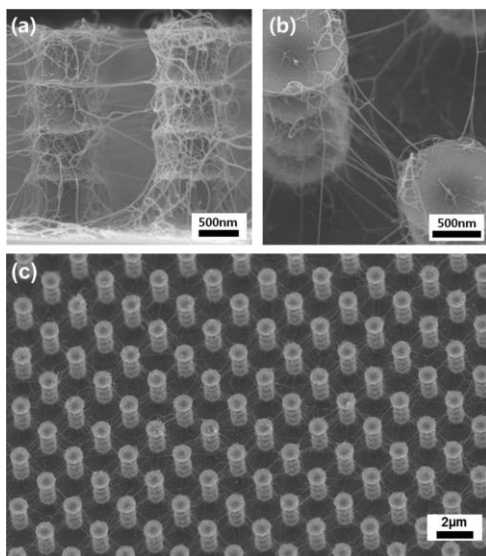

Figure 2-2. SEM images of (a) cross-sectional, (b) tilted images of interconnected SWNTs on the Si pillar surface, and (c) the uniformly networked SWNTs on the whole substrate.

Figure 2-3. TEM image of interconnected CNTs on the Si pillar surface.
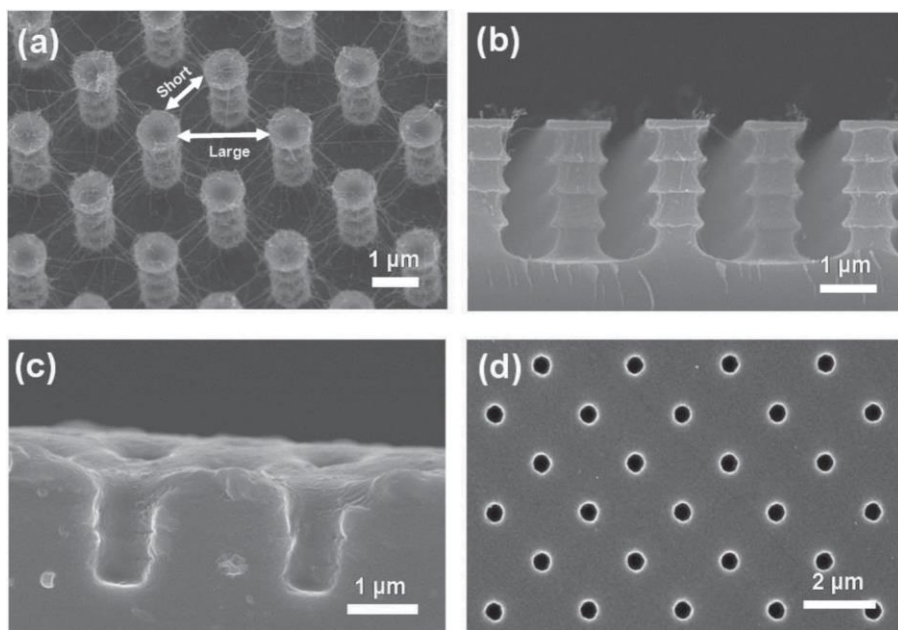

Figure 2-4. SEM images of a) 3D network of SWNTs, b) Si pillar arrays after removing the 3D network of SWNTs by a lifting-up process, and c) the SWNT-PDMS film. d) Top view SEM image of the 3D network of SWNTs in PDMS.

A tilted image of the 3D network of SWNTs on a pillar substrate is displayed in **Figure 2-2**a. The SWNTs were interconnected between adjacent Si pillars over their entire length with a small gap, and a few SWNTs were formed between two Si pillars separated by a large gap, as reported previously. In addition, Figure 2-2a shows that CNTs were grown along the pillar surface. Each interconnected CNT was made up of a bundle of SWNTs (Figure 2-2b). Based on the TEM

analysis, an average of 10 SWNTs was suspended between two adjacent Si pillars with a small gap (Figure 2-3). An SEM image of the substrate after PDMS infiltration and the subsequent peeling off procedure is shown in Figure 2-4b. The PDMS has good wettability on the CNTs and thus, hierarchically ordered 3D networks of SWNTs were well embedded in the PDMS. Consequently, a 3D network of SWNTs was maintained even after detaching the structure from the Si pillars along with PDMS. Most of the SWNTs on the surface were removed and only a small portion was left on the edge of the pillars. The PDMS film embedded with a 3D network of SWNTs is shown in Figure 2-4c and 4d. The holes in the PDMS film were formed by the Si pillars, and these holes shrunk because of the elastomeric property of the PDMS. Raman analysis with a micro-sized laser-beam was conducted at a position between two adjacent holes in the PDMS film (Figure 2-5a). As shown in Figure 2-5b, the Raman spectra indicate that SWNTs existed in the film. The analytical point and Raman spectrum of exposed CNTs on the surface of the inner hole in the PDMS film are displayed in Figure 2-6. The Raman spectrum obtained in radial breath mode (RBM) revealed that SWNTs were exposed in the hole in the PDMS film.
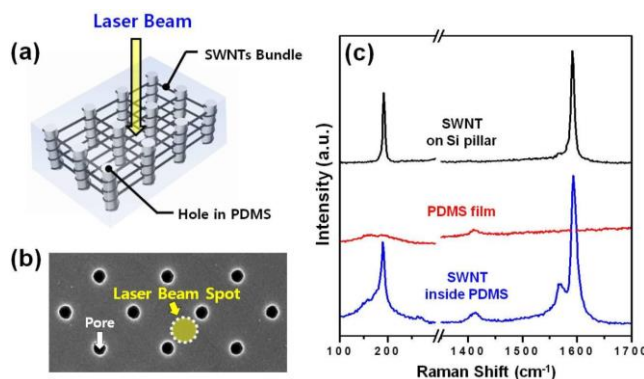

Figure 2-5. (a) Location of analysis points for the Raman spectra. (b) Top-down SEM image of SWNTs embedded in a PDMS film and the description of the laser point on the PDMS film. (c) Raman spectra for the 3D network of SWNTs embedded in PDMS film.
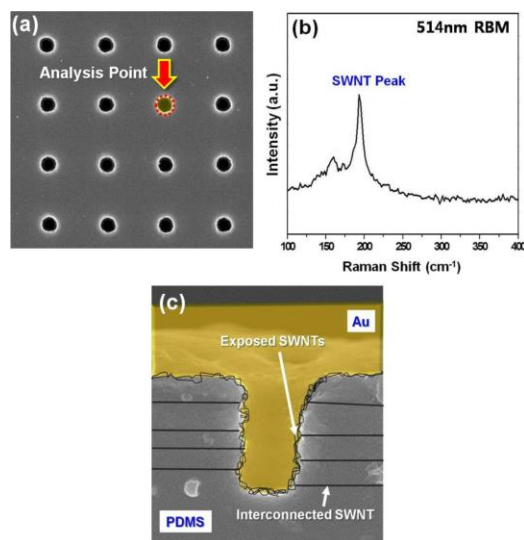
Figure 2-6. (a) Top-down SEM image of the 3D network of SWNTs embedded PDMS film and description of the laser point on the PDMS film. (b) Raman spectrum of exposed SWNTs in the pore of the PDMS film. (c) Schematic of the Au electrode and interconnected SWNTs in the pore of the 3D network of SWNTs embedded PDMS film.
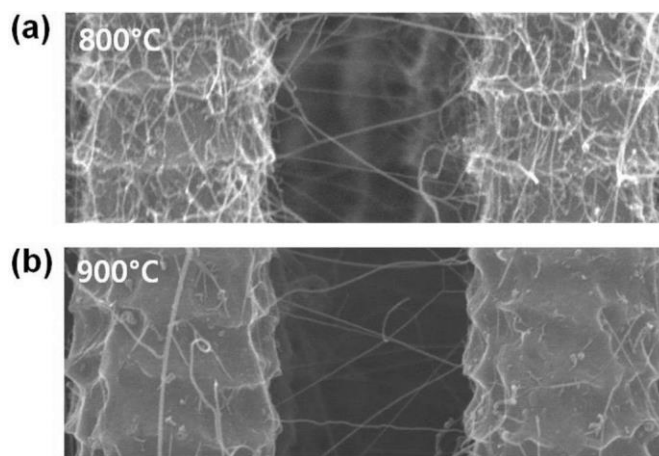

Figure 2-7. Density of SWNTs on the pillar surface depending on synthesis temperature; (a) 800°C and (b) 900°C

In order to operate PDMS film as a sensor, which has an embedded, ordered CNT network, the whole film should be interconnected electrically. The growth of CNTs on the pillar surface is important to fabricate the sensor, facilitating growth of internetworked CNTs between pillars. Figure 2-7 shows that the interconnected SWNTs were electrically connected with CNTs on the pillar surfaces. The CNTs on the Si pillar surfaces led to the construction of an effective electrical network. When the CNTs were synthesized at 900 °C, the CNTs preferentially grew directly onto adjacent pillars, as shown in Figure 2-3b. In this case,

although the CNTs were embedded in the PDMS film, the film was not conductive because the number of CNTs which provide electrical paths on the pillar surface was insufficient to conduct electricity. Figure 2-S8 shows a typical current– voltage (*I–V*) response curve, which clearly exhibited Ohmic contacts between interconnected SWNTs in the film. The resistance of the film was in the range of $\oplus 10^4$ $\wedge$.
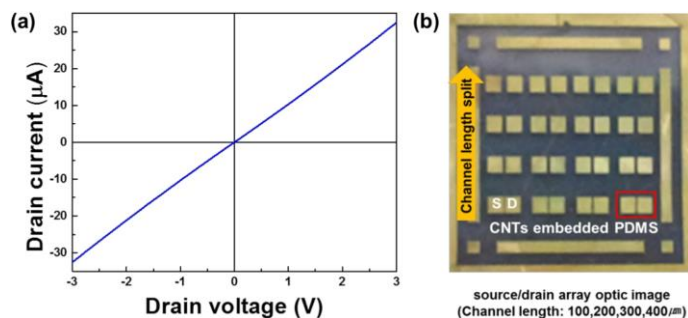

Figure 2-8. (a) I–V curve and (b) optic image of gold electrodes of the 3D network of SWNTs embedded in PDMS.

A plot of $\Delta R/R_0$ versus time for four stretching cycles is shown in **Figure 2-9**a. The applied tensile strains were 0.5%, 1.0%, 2.0%, and 3.0%, respectively. With the application of a 1% strain, $\Delta R/R_0$ changed by 0.35. When 1% strain was applied to the sensor, the representative index of sensitivity of the strain sensor, also known as the gauge factor (GF, defined as: $(\Delta R/R_0)/\Sigma$), was 35. The GF value of this sensor is higher and more stable than that of conventional strain sensors based on metal alloys (GF = 2.0) and CNT/polymer composites (GF = 0.06–6.82).
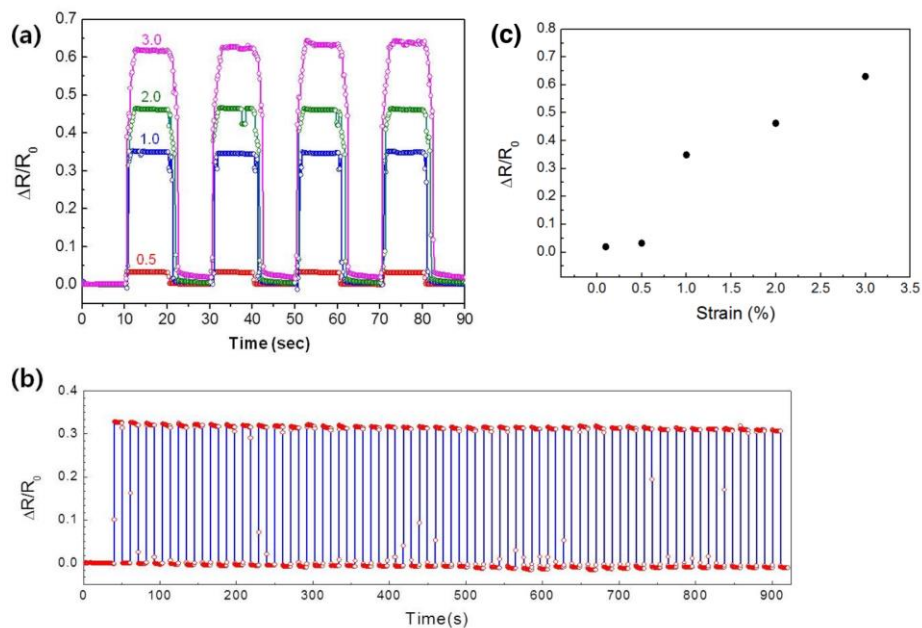
Figure 2-9. Resistance characteristics of the 3D network of SWNTs in PDMS. a) Resistance under an applied tensile strain of 0.5% to 3.0%. b) Reliability of the resistance under an applied tensile strain of 1.0%. c) The relative change in electrical resistance versus mechanical strain.

As shown in Figure 2-9c, the mechanical stability of the sensor film was maintained after repeated 1% tensile strain. This procedure was repeated at least 50 times. It was con- firmed that the sensor device showed very stable operational characteristics in terms of signal reproducibility. When the sensor was returned to the relaxation state, $\Delta R/R_0$ was recoverable. In addition, the sensor shows a fast response to applied and released strains, and the $\Delta R/R_0$ peak was constant during the applied strain for 10 s.

Figure 2-10 shows the Raman spectra of the embedded 3D network of SWNTs in the PDMS film under applied strains of 0.5, 1.0, 2.0, and 3.0%. Through the use of Raman spectroscopy, it is possible to analyze the band structure of the SWNTs based on the change in SWNT deformation The results showed that the RBM was not affected by the applied strain in the film. However, the wavenumber of the disorder induced, as evaluated by the D* band (located at 2607 cm ^{1}, also termed G2), was shifted downwards (Figure 2-10b). Even though there is no chemical functionalization of 3D network of SWNTs, a bonding between the SWNTs and the PDMS is evident by the marked Raman shift with strain. An empirical linear relation- ship exists between

the SWNT D* wavenumber shift and the applied elastic strain. If the nanotube D* wavenumber difference between the zero strain state and the applied strain (ε) state is defined as the Raman wavenumber shift ($\Delta\omega$), the empirical slope (m) of the wavenumber-strain relation can be defined from

$$\Delta\omega = m \cdot \varepsilon \tag{1}$$

As seen in Figure 2-7, the slope (m) in the elastic regime is –351 cm[1] per strain. The slope is a critical parameter for strain mapping by Raman spectroscopy, and it is affected by the matrix properties and the orientation of the nanotubes with respect to the principal strain axis.
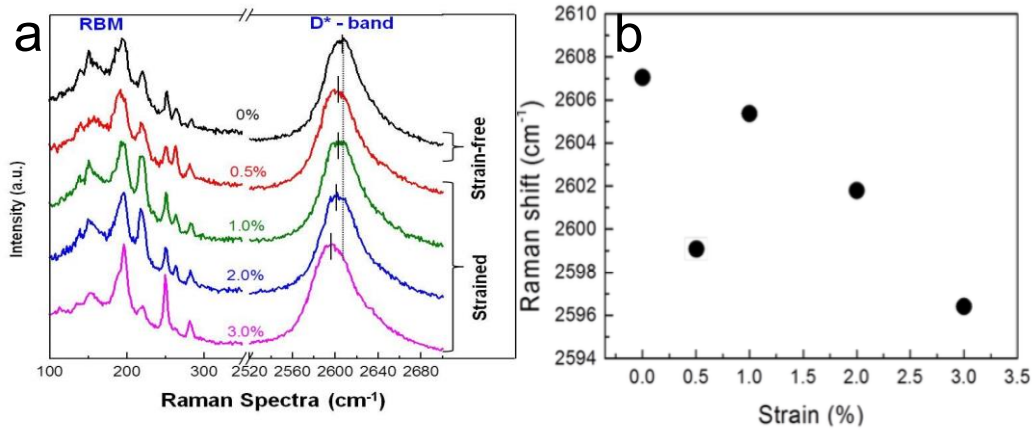

Figure 2-10. (a) Raman spectra of the 3D network of SWNTs in PDMS; the shift in the D*-band modes in the SWNT-PDMS film is shown as a function of the tensile strain. (b) Raman shift of the D*-band modes of the 3D network of SWNTs in PDMS as a function of the tensile strain.

Young et al. Proposed a simple model for the dependence of the carbon fiber strain ε (θ) on the carbon fiber orientation θ based on the assumption that the fiber and matrix strains are equal in the center of a fiber aligned parallel to the tensile axis. The model, which simply reflects the classical strain transformation equations in elasticity theory, is expressed as follows

$$\varepsilon_{real} = \varepsilon_{o}(\cos^2\theta - v\sin^2\theta) \tag{2}$$

where v is the Poisson's ratio of the matrix. It is assumed that Poisson's ratio of the PDMS (1:10 mixing ratio) is 0.5, and that the SWNT angle in our strain sensor, angle (θ), is 45° and

DISTRIBUTION A: Approved for public release: distribution unlimited.

45° (Figure 2-11). According to Equation (1), a real applied strain value on the interconnected SWNTs (ε_{real}) is approximately $1/4\varepsilon_o$.
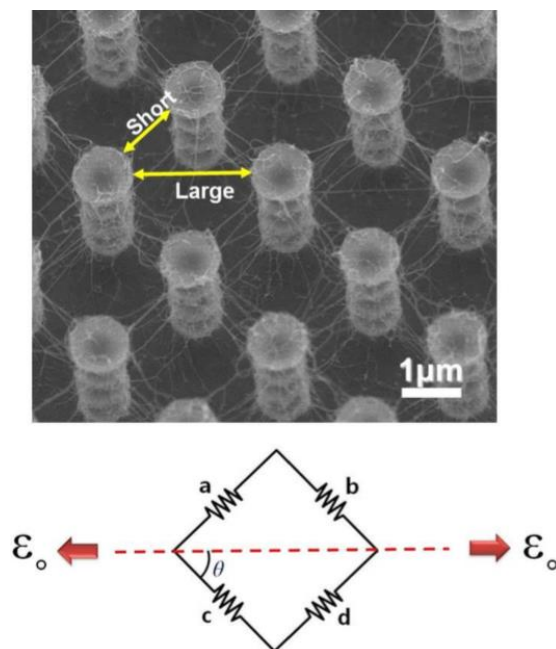

Figure 2-11. Schematic representation of an off-axis carbon nanotube at an angle.

With the application of a 0.5% strain, the D* band was shifted 8 cm^{-1}. This value is similar result of Young et al., which the SWNTs were distributed into a matrix resulting in a low volume fraction (<0.1 wt%). During the initial strain state, 0.5% strain, the SWNTs was deformed while the network of SWNTs was stretched because of the strong bonding each other between SWNTs and PDMS. However, 1% strain was applied to the sensor, the D* band was shifted a little more than the 0.5% strain state. In contrast, 0.5% and 1% strain applied to the sensor, $\Delta R/R_0$ changed from 0.0319 and 0.35, respectively (Figure 2-9b). From this comparison, it cannot be assumed that ΔR of this sensor was affected by deformation of SWNTs. To elucidate the results of the sensor, it has to be considered that the effect of the interface separation during part of the cycle. At higher than 1% strain values, the nanotubes were slightly detached from the surrounding PDMS. It can confirm through the decrease of the shift value of D* band. The detachment is more critical on the junction point of the nanotubes. Thus, the electrical conductivity of the sensor is affected by the tensile stress at higher than 1% strain values. In previous reports, strain sensors formed with a random network of SWNTs showed an irrecoverable loss of the junctions between the CNTs since

the reorientation of CNTs after slippage of nanotubes within agglomerates during loading. And thus, the resistance reliability under applied tensile strains as a function of time was not acceptable. However, the 3D network of SWNTs in this work is well interconnected and maintained in the PDMS as an external tensile force is applied. The ordered 3D network is arranged with suspended CNTs which are evenly spaced between CNTs. Hence, PDMS is able to fully wrap the individual CNTs so that as the sensor is subjected to a certain degree of strain, PDMS can evenly influence the individual CNTs. Also, when the film comes back to its original state after the strain, the CNT position will not change.

Repeat and validation

All our previous data were obtained from only one-type of samples. Even though we have done some works repeatedly, all data were not as good as previous one. In Figure 2-12, the resistance difference during stretching process was not clearly notified. The sensing repeatability of CNTs embedded in PDMS was not satisfied compared to previous data. Therefore, here we cannot provide reliable and repeatable data with 3DNC embedded in PDMS.

However, by using another strain sensor of SWNTs embedded in PDMS both densely grown SWNTs on flat silicon wafer and pillar structure, SWNTs embedded in PDMS, the measurement data were better than that those obtained from our 3DNCs as shown in figures 14 and 15. But they are still not as good as our previous data. In Figure 2-15a and 16b we can see that resistances are not consistent at release state. At different stretching states, the base resistance changed. However previous data are not consistent. Another serious problem is that even during stretching or releasing state, the resistance value was also not stable continually. In addition, the calculated gauge factor ε ($\varepsilon = 4.44$ and 1.83 for Figure 2-15a and 16b, respectively) are much lower than our previous data ($\varepsilon = 35$).
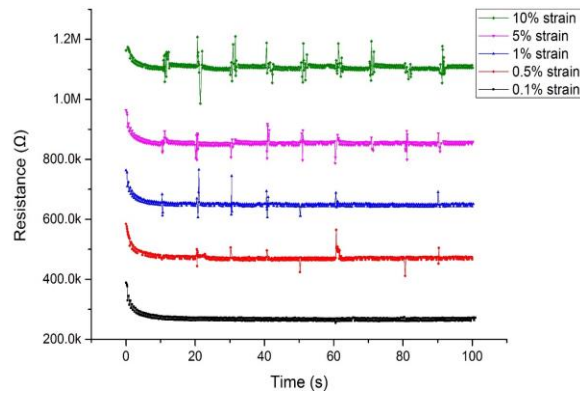
Figure 2-12. Resistance characteristics of the 3D network of SWNTs embedded in a PDMS film
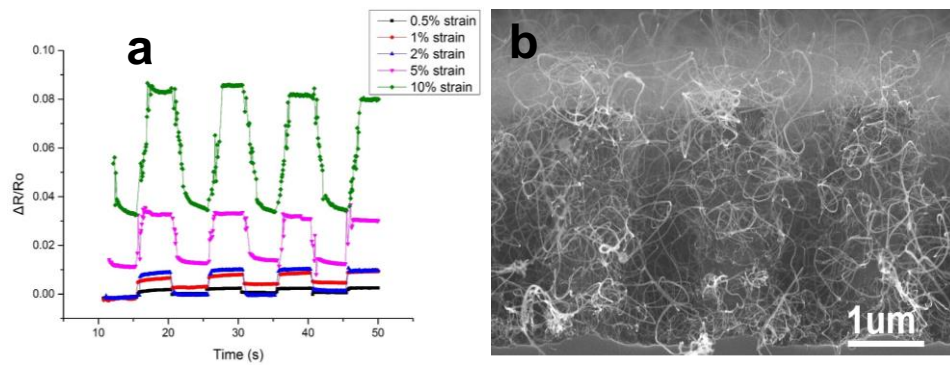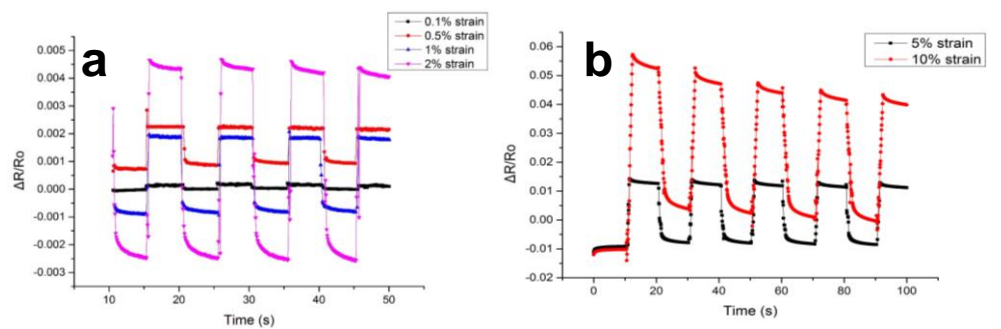

Figure 2-13. (a) Resistance characteristics of the CNTs embedded in a PDMS film under applied tensile strains of 0.5 to 10 %; (b) SEM images of densely growned CNTs on pillar structure.
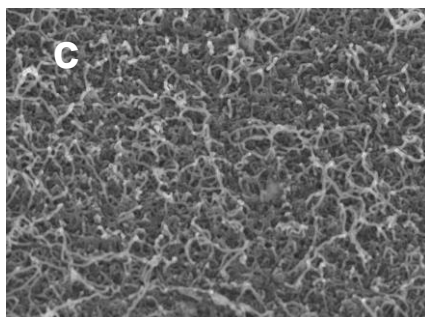
Figure 2-14. (a) and (b) Resistance characteristics of the 3D network of SWNTs embedded in a PDMS film; (c) SEM images of densely growned CNTs on flat silicon wafer.
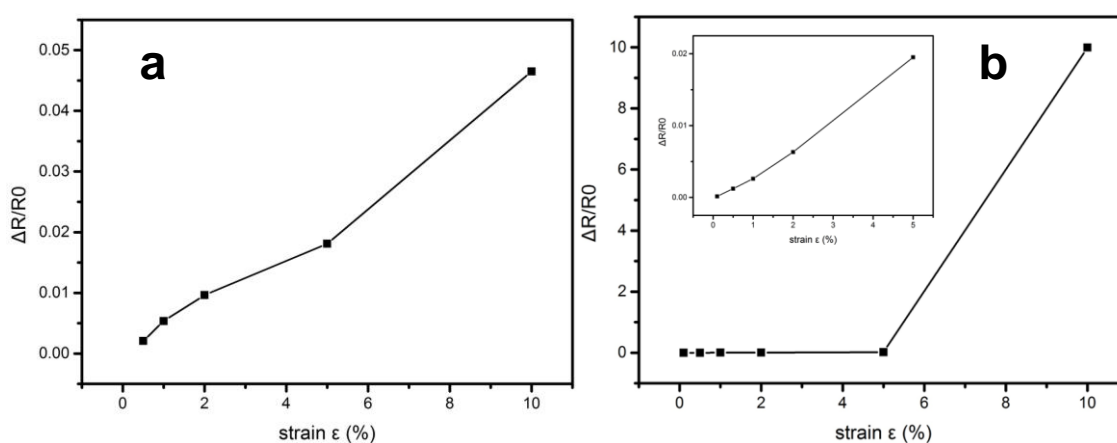

Figure 2-15. (a) The relative change in electrical resistance versus mechanical strain of densely growned CNTs on pillar structure. (b) The relative change in electrical resistance versus mechanical strain of densely growned CNTs on flat silicon wafer.

By continuous repeating experiments, its poor repeatability was the problem comes from its poor connection between CNTs embedded in PDMS and outer gold electrode layer. In the PDMS holes there are few exposed CNT tails (the amount is determined by the number of CNTs grown on pillar surface), which plays an important role in connecting embedded CNT network and outer electric circuit (Figure 2-16b). In our previous preparation process after peeling off, the PDMS was directly coated with a layer of Au (100nm) as shown in Figure 2-16a. Figure 2-16c and 18d showed that coated Au are always in particle form and it is very hard for them to be deposited uniformly inside the PDMS holes which directly leading to the problem that hindered our progress for so long time. At the same time, the exposed CNT tails are always covered with a layer of PDMS, and it means that even the deposited gold particles were contacted with CNT tails, the connection between CNT and gold is still not in good condition.
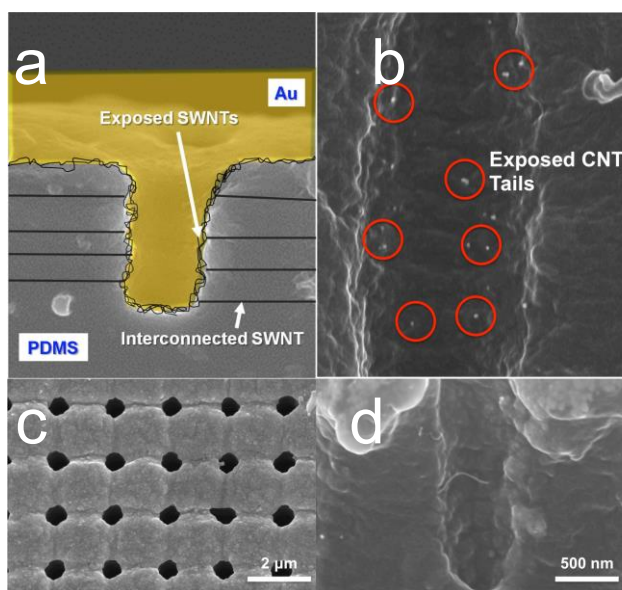
Figure 2-16. Comparison ideally Au coated PDMS and practically Au coated PDMS. (a) is the ideally Au coated PDMS; (b) shows the exposed CNT tails on the inner wall of PDMS holes; (c) and (d) shows practically Au coated PDMS.

To solve this problem, our fabrication process was upgraded as shown in Figure 2-17d. After peeling off, silver nanoparticles (<20nm) were firstly applied to fill the holes in electrode part, which may give a better connection with the exposed CNT tails.
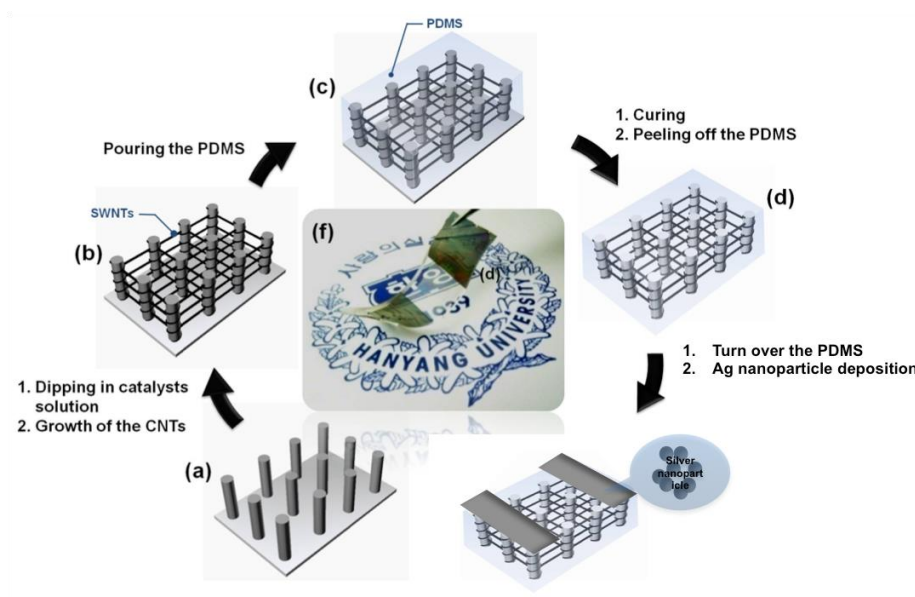

Figure 2-17. Schematic illustration of the improved fabrication process for solving previous problems.

DISTRIBUTION A: Approved for public release: distribution unlimited.

After peeling, PDMS was firstly treated with O_2 plasma for improving hydrophilicity as silver nanoparticles were dissolved in aqueous solution. Then silver nanoparticles were uniformly wiped on the electrode area and dried under vacuum for 24h. Then sample was set on a hot plate under 140°C for 1h. Figure 2-18 shows a cross-section view of SEM image of silver coated area. Silver nanoparticles were successfully filled into the holes and deposited well in the hole. Thus, CNT tails were covered and connected by those silver particles. Figure 2-19 shows the strain test of silver nanoparticle coated PDMS/3DNC. Stretching and releasing interval were 10s and 10s, respectively. The resistance was still unstable at stretching and releasing states. The resistance of pristine PDMS/3DNC was also very large with a value of more than 400 KΩ. This is because of the oxidized form of silver nanoparticles during a drying step at the temperature of 140℃. However, in our previous report, the resistance value change at stretching and releasing states was very clear and distinctive, and the value was only ~10 KΩ as shown in Figure 2-13.

The problem of electrode contact was not an issue in the paper published in Advanced Materials entitled "*A Highly Sensitive and Reliable Strain Sensor Using a Hierarchical 3D and Ordered Network of Carbon Nanotubes*". But, a prolonged effort for finding a way for overcoming this contact problem issue is needed.
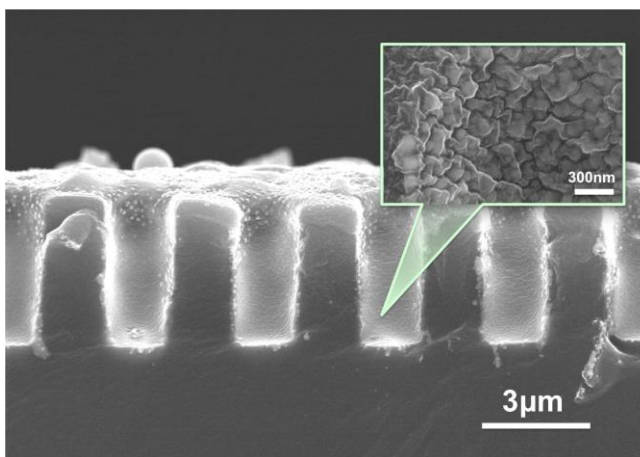

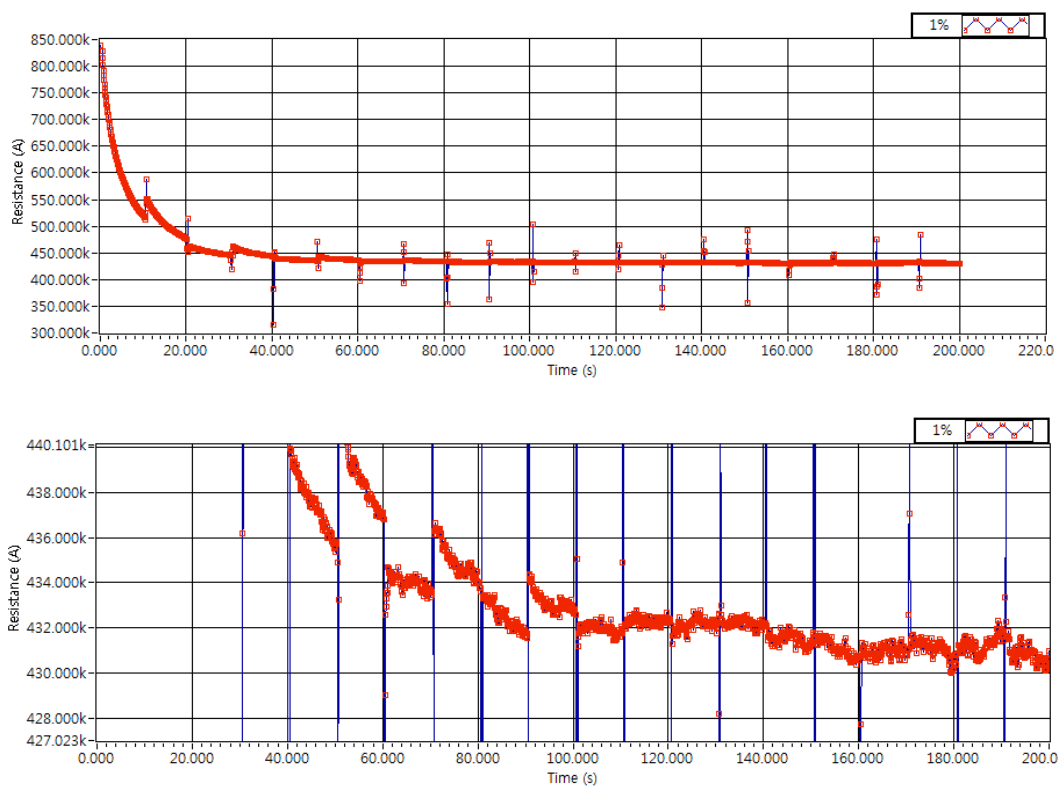**Figure 2-18. SEM of silver nanoparticle coated PDMS.**

Figure 2-19. Strain test of silver nanoparticle coated PDMS/3DNC at 1% strain.

List of Publications and Significant Collaborations that Resulted from this AOARD Supported Project

a) papers published in non-peer-reviewed journals and conference proceedings

1. Seo J, Lee T J, Lim C, et al. A Highly Sensitive and Reliable Strain Sensor Using a Hierarchical 3D and Ordered Network of Carbon Nanotubes[J]. **Small**, 2015.
2. Lee, K. G.; Lee, S.; Chang, S. J.; Choi, B. G.; Seo, J.; Sangalang, A.; Kim, D. H.; Park, T. J.; Lee, M. K.; Lee, S. J.; Lee, H., Bio-inspired Hierarchcal Nanowebs for Green Catalysis, **Small**, **2015**, 11, 34, 4292-4297

b) conference presentations without papers

1. Seok Jin Jo, Chen Rui, Jeongeun Seo, Yong Deok Jo, Haiwon Lee, Silicon Pillar Array Sructure Assisted Fabrication of Three-dimensional Manganese Oxide Net by Electrochemical Deposition for Supercapacitor Applications, **ChinaNANO 2015**, 2015
2. Jeongeun Seo, Chen Rui, Seok Jin Jo, Yong Deok Jo, Haiwon Lee, A Highly Sensitive and Reliable Strain Sensor using Hierarchical Three-dimensional Network of Carbon Nanotubes, **AsiaNANO 2014**, 2014
3. Jo, Y.; Lee, S. K.; Seo, J.; Lee, S.; Lee. H., Three-dimensional Network of TiO2 coated Carbon Nanotubes for NH3 Gas Sensor, **NANO KOREA 2013**, 2013
4. Lee, H., Hierarchical Three-dimensional Network of Carbon Nanotubes for Biosensor Applications, **2013 INST Symposium "Bioinspired Namomaterials and Systems"**, 2013
5. Lee, H., Hierarchical and Multifunctional Three-dimensional Network of Carbon Nanotubes of Sensor Applications, **College of Engineering Forum on Interfacial Science and Biotechnology,** 2013
6. Lee, H., Hierarchical and Multifunctional Three-dimensional Network of Carbon Nanotubes for Early Diagnosis, **SPIE 2013 Nano-Bio Sensing, Imaging &**

Spectroscopy, 2013

7. Seo, J.; Cho, S.; Jo, Y. D.; Kim, S.; Lee, H., Hierarchical and Multifunctional Three-dimensional Networks of Carbon Nanotubes for Microfluidic Filtration, **AsiaNANO2012**, 2012

8. "Hierarchical Three-dimensional Network of Carbon Nanotubes for Biosensor Applications", **2013 INST Symposium**, Hanyang University, Seoul, July 9th, 2013

c) Provide a list any interactions with industry or with Air Force Research Laboratory scientists or significant collaborations that resulted from this work.